

Article

Wavelet Analysis of Atmospheric Ozone and Ultraviolet Radiation on Solar Cycle-24 over Lumbini, Nepal

Prakash M. Shrestha ^{1,2}, Suresh P. Gupta ¹, Usha Joshi ^{1,2}, Morgan Schmutzler ³, Rudra Aryal ^{3,*}, Babu Ram Tiwari ⁴, Binod Adhikari ⁵, Narayan P. Chapagain ⁶, Indra B. Karki ¹ and Khem N. Poudyal ⁴

¹ Department of Physics, Patan Multiple Campus, Tribhuvan University (TU), Lalitpur 44700, Nepal; prakash.shrestha@pmc.tu.edu.np (P.M.S.); usha.joshi@pmc.tu.edu.np (U.J.); indra.karki@pmc.tu.edu.np (I.B.K.)

² Central Department of Physics, Tribhuvan University (TU), Kritipur 44618, Nepal

³ College of Health and Natural Sciences, Franklin Pierce University, Rindge, NH 03461, USA; schmutz-lerm20@live.franklin Pierce.edu

⁴ Department of Applied Sciences and Chemical Engineering, Pulchowk Campus, Tribhuvan University (TU), Lalitpur 44700, Nepal

⁵ Department of Physics, St. Xavier's College, Tribhuvan University (TU), Kathmandu 44613, Nepal

⁶ Department of Physics, Amrit Campus, Tribhuvan University (TU), Kathmandu 44613, Nepal

* Correspondence: aryalr@franklin Pierce.edu

Abstract: This research aims to comprehensively examine the clearness index (K_T), total ozone column (TOC), and ultraviolet A (UVA) and ultraviolet B radiation (UVB) over Lumbini, Nepal ($27^\circ 28' N$, $83^\circ 16' E$, and 150 m above sea level) throughout the 11 years of solar cycle 24 (2008 to 2018). The Lumbini, a highly polluted region, is important in advancing the identification and analysis of TOC variations across regions with similar geographical and climatic attributes. Data from the Ozone Monitoring Instrument (OMI) of the EOS-AURA satellite of NASA were used to analyze the daily, monthly, seasonal, and annual trends in the clearness index (K_T), ultraviolet A (UVA), ultraviolet B (UVB), and TOC from the Comprehensive Environmental Data Archive (CEDA). The study found that the yearly averages for K_T , TOC, UVA, and UVB were 0.55 ± 0.13 , 272 ± 14 DU, 12.61 ± 3.50 W/m², and 0.32 ± 0.11 W/m², respectively. These values provide insights into the long-term variations in atmospheric parameters at Lumbini. The study also applied the continuous wavelet transform (CWT) to analyze K_T , TOC, UVA, and UVB temporal variations. The power density peak of 35,000 DU² in the TOC was observed from the end of 2010 to the end of 2011, within 8.5 years, underscoring the significance of analyzing TOC dynamics over extended durations to understand atmospheric behavior comprehensively.

Keywords: clearness index; total ozone column; Dobson unit; ozone depletion; UV



Citation: Shrestha, P.M.; Gupta, S.P.; Joshi, U.; Schmutzler, M.; Aryal, R.; Tiwari, B.R.; Adhikari, B.; Chapagain, N.P.; Karki, I.B.; Poudyal, K.N.

Wavelet Analysis of Atmospheric Ozone and Ultraviolet Radiation on Solar Cycle-24 over Lumbini, Nepal. *Atmosphere* **2024**, *15*, 509. <https://doi.org/10.3390/atmos15040509>

Academic Editors: Enrico Ferrero, Elvira Kovač-Andrić and Abd Al Karim Haj Ismail

Received: 30 January 2024

Revised: 21 March 2024

Accepted: 14 April 2024

Published: 21 April 2024



Copyright: © 2024 by the authors. Licensee MDPI, Basel, Switzerland. This article is an open access article distributed under the terms and conditions of the Creative Commons Attribution (CC BY) license (<https://creativecommons.org/licenses/by/4.0/>).

1. Introduction

The sun emits electromagnetic waves from 100 nm to 400 nm, with UV radiation categorized into UVC (wavelength range: 100 nm to 280 nm), UVB (wavelength range: 280 nm to 315 nm), and UVA (wavelength range: 315 nm to 400 nm) [1,2]. These different types of radiation have varying effects on human health, with shorter wavelengths posing higher risks [3]. The importance of understanding UV radiation lies in its impact on human health, particularly as shorter wavelengths have lower penetration capability through the skin [4]. Atmospheric ozone, with the chemical formula O₃, protects Earth's surface from UV radiation. Previous studies have presented the intricate mechanisms involved in ozone formation and breakdown, emphasizing the role of atmospheric processes that protect our planet [5,6]. Approximately 90% of atmospheric O₃ is concentrated within the stratosphere, serving as a critical shield against harmful ultraviolet radiation. O₃ effectively absorbs all UVC radiation and a significant portion of UVB, permitting a substantial fraction of UVA

radiation to reach the Earth's surface, where UVA is less biologically damaging than UVC and UVB [1,2,6–12].

Solar UV radiation induces chemical transformations in the troposphere, leading to beneficial and harmful consequences. Photochemical smog, formed by urban pollutant gases exposed to UV radiation, causes millions of premature deaths globally. Conversely, UV radiation improves air quality by generating hydroxyl radicals that remove various gases relevant to stratospheric ozone, climate, and air quality [13,14]. The interconnected effects of stratospheric O₃ depletion, UV radiation, and climate change are evaluated regarding air quality, carbon sinks, ecosystems, human health, and materials. Tropospheric O₃ significantly impacts the atmosphere's radiative budget and oxidation capacity [15]. Black carbon and tropospheric O₃, both short-lived climate forces, negatively affect global and regional air quality and contribute to climate change [16–18]. The evolution of terrestrial plant life is linked to the development of the O₃ layer as an external UV screen. The O₃ layer's depletion, particularly over Antarctica, is attributed to manufactured CFCs, resulting in the formation of the "O₃ hole" [19,20]. The role of nitrogen oxides in catalytic reactions is also critical for atmospheric ozone balance emphasizes the importance of understanding and mitigating anthropogenic impacts on the O₃ layer [21]. The increased temperature in the lower troposphere and higher concentrations of NO and NO_x contribute to chain reactions that play a significant role in atmospheric processes [22,23]. Photochemical production of O₃ in the troposphere is variable and depends on the NO_x concentration, which is influenced by factors like methane and other hydrocarbons. Additionally, previous studies also suggest that region-specific analyses are necessary to understand ozone dynamics in different latitudinal zones, as O₃ distribution is influenced by atmospheric dynamics, geographical location, and climatic variables in a complex manner [24].

Utilizing a wavelet analysis technique on K_T, TOC, UVA, and UVB variables provide valuable insights into both their frequency and time-based variations. This analysis method breaks down the time-series data into components that reveal patterns, frequencies, and trends that may not be immediately apparent in the raw data. Studies have shown that this approach can help to uncover important information that would otherwise remain hidden [25–27].

Monitoring O₃ dynamics is essential as O₃ plays a vital role in shielding the Earth from harmful UV radiation. Changes in the ozone layer can have implications for human health, ecosystem well-being, and climate. The interplay between ozone, UV radiation, and solar cycles contributes to our understanding of climate change dynamics. Changes in solar activity and their impact on atmospheric components can have cascading effects on climate patterns, emphasizing the need to study and comprehend these relationships for accurate climate modeling and prediction.

2. Methodology

2.1. Site Description

Nepal is a landlocked country in Southwest Asia, known for its mountainous terrain. It spans latitudes from 26.36° N to 30.45° N and longitudes from 80.06° E to 88.2° E, exhibiting diverse topography. With elevations ranging from 60 m to 8848 m, the country covers a vertical span of 200 km from south to north and extends around 800 km from east to west. Nepal is located between India and China, both large industrial countries. Industrial activities in these neighboring countries can significantly impact the O₃ levels in the atmosphere, leading to depletion over the region [28–31]. Therefore, conducting a detailed study of atmospheric concentrations is important to understanding and mitigating the potential effects of industrial activities on O₃ levels in Nepal.

Lumbini is located near the northern edge of the central Indo-Gangetic Plain (IGP), a region with high levels of air pollution load. As a result, Lumbini is heavily impacted by air pollution transported from the IGP region [28,29,32]. Several pollutants, including NO_x and volatile organic compounds (VOCs), known as O₃ precursors, are released around Lumbini, and studies in different regions have shown that when these substances react

in sunlight, they undergo photochemical reactions that produce ozone. These reactions are particularly prevalent in densely populated urban and industrial areas with high emission levels [23,31,33]. Figure 1 shows the location of the Lumbini region on a map of Nepal [34]. The average annual maximum temperature in Lumbini is 31.8 °C, while the average annual minimum temperature is 18.7 °C. The region receives an average of 1369.5 mm of rainfall [35].

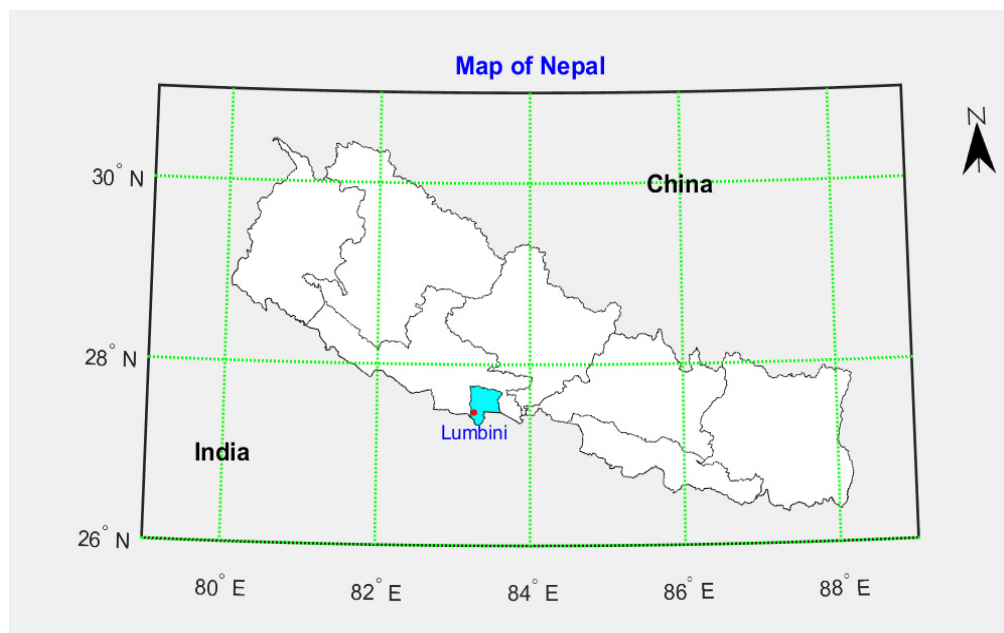


Figure 1. Map of Nepal and Lumbini.

2.2. Data Analysis and Data Analytic Tools

Data on the daily TOC spanning solar cycle 24 (2008 to 2018) were obtained from Ceda Archive [36]. At the same time, daily data for the K_T , UVA, and UVB were acquired from NASA's data access viewer at the Power project [37]. The dataset utilized in this study is structured on a 1-degree geographic grid, encompassing an area spanning approximately 100 km by 100 km. The data analysis and graphical representation were conducted using open-source Python 3.7 software on the Anaconda 3 platform (Jupyter Notebook) for calculation and plotting [38]. K_T is a measure of the ratio of terrestrial solar radiation (H_g) on the ground to extraterrestrial solar radiation (H_0) in Earth's outer atmosphere. The statistical parameters used to present the results were the mean ($\bar{x} \pm$ standard deviation (σ), with the standard error (SE) being used as the error bar in the graphs. The coefficient of variation (CV) was used as a metric to evaluate the data's variability. To gain a deeper understanding of the atmospheric parameters being studied, we employed statistical tools as defined in [39] such as quartiles (Q_1 , Q_2 , Q_3), skewness (γ_1), and kurtosis (γ_2) to scrutinize the distribution of K_T , TOC, UVA, and UVB. These comprehensive analyses help to identify the variability and distribution characteristics of these parameters [39].

The daily mean of the TOC can also be analyzed to observe seasonal variation by using Fourier series [40].

$$y_s = a_0 + a_1 \cos\left(\frac{2\pi}{365} n_d\right) + b_1 \sin\left(\frac{2\pi}{365} n_d\right) \quad (1)$$

where n_d is the number of the day of the year, a_0 is the offset, and the amplitude of the seasonal component is $\sqrt{a_1^2 + b_1^2}$.

In this study, we used four seasons: pre-monsoon (March–May), monsoon (June–September), post-monsoon (October–November), and winter (December–February). The coefficient of relative variation (CRV) is given by,

$$CRV_i = \frac{x_i^{max} - x_i^{min}}{x_i^{mean}} \times 100 \quad (2)$$

where x_i^{max} , x_i^{min} , and x_i^{mean} denote the maximum, minimum, and mean of data in i th day, respectively.

The continuous wavelet transform (CWT) is a tool for analyzing localized variations in energy within a time series by dividing into wavelets. The continuous wavelet transform of function $f(t)$ is cross-correlation with a function $\psi((t - b)/a)$ [40,41].

$$W(a, b) = \frac{1}{\sqrt{a}} \int f(t) \psi \left(\frac{t - b}{a} \right) dt \quad (3)$$

Here, the asterisk is a complex conjugate. “ a ” represents the dilation and contraction of the wavelet, and “ b ” is the translation in time t . The Morlet wavelet consisting of function $\psi(t)$ [42]

$$\psi(t) = \frac{1}{\pi^{1/4}} e^{i\omega t} e^{-t^2/2} \quad (4)$$

where ω represents the dimensionless frequency. $|W(a, b)|^2$ represents the wavelet power spectrum (WPS). The average wavelet power (also known as the global wavelet power spectrum (GWS)) is the average variation in the whole time series on every scale [43].

$$GWS = \int |W(a, b)|^2 dt \quad (5)$$

3. Results and Discussion

Daily data for the TOC K_T , UVA, and UVB were used for analyzing monthly, seasonal, and annual variations. Figures 2–9 are presented for this analysis of atmospheric O_3 and UV radiation on solar cycle 24 over Lumbini, Nepal. Furthermore, the variations in the dataset were analyzed using the wavelet transform technique, presenting the temporal dynamics of atmospheric parameters illustrated in Figure 9.

Figures 2a and 3a show the daily variation and histogram of the clearness index (KT), respectively. The peak value of 0.79 was observed on 10 April 2017, while the minimum value of 0.06 was recorded on 21 June 2016. Based on 11 years of data, the average clearness index was determined to be 0.55 ± 0.13 . Key statistical measures were identified as follows: Q_1 was 0.48, Q_2 was 0.59, and Q_3 was 0.66. The data distribution in the study shows a skewness of -0.91 and a kurtosis of 0.44. These values suggest that the distribution was negatively skewed and deviated from Gaussian normality. Out of the 4015 days studied, 1211 days had a clearness index between 0.6 and 0.7. Also, 309 days were classified as cloudy ($K_T < 0.34$), while 1241 days were categorized as clear ($K_T > 0.65$). The graphs from Figures 2b and 3b show the daily changes and histograms of the TOC. On 4 February 2010, the TOC reached its highest value of 331 DU, while its lowest of 220 DU was recorded on 17 December 2018. The average TOC over the 11 years was determined to be 272 ± 14 DU. The distribution’s first quartile, second quartile, and third quartile were identified as 263 DU, 271 DU, and 281 DU, respectively. The distribution of the TOC was positively tailed, deviating from Gaussian normality, with a skewness of 0.10 and kurtosis of 0.42. It was observed that out of the 4015 days in the study period, 2204 days’ worth of TOC values fell within the range of 260 DU to 280 DU.

Figures 2c and 3c display the daily variation and histogram of ultraviolet A (UVA), respectively. On 9 June 2010, UVA reached a maximum value of 20.79 W/m^2 , and it reached a minimum of 2.31 W/m^2 on 9 January 2012. The average UVA value for the 11 years was $12.61 \pm 3.50 \text{ W/m}^2$. The key statistical measures, including the first, second, and third

quartiles, were identified as 9.87 W/m^2 , 12.88 W/m^2 , and 15.27 W/m^2 , respectively. The distribution of UVA was negatively skewed, with a skewness of -0.17 and a kurtosis of -0.64 . This indicates a negatively tailed distribution that deviates from Gaussian normality. Notably, during the study period, 846 days recorded UVA values between 14 W/m^2 and 16 W/m^2 . These analyses provide insights into daily, monthly, and annual variations in clearness index, total ozone column, and UVA. Figures 2d and 3d present the daily variation and corresponding histogram of ultraviolet B (UVB), respectively. The highest recorded UVB value was 0.57 W/m^2 on 14 July 2009, while the lowest value of 0.04 W/m^2 was recorded on 9 February 2010. Over the 11-year study period, the average UVB rate was calculated to be $0.32 \pm 0.11 \text{ W/m}^2$. Key statistical measures were identified with the first, second, and third quartiles at 0.22 W/m^2 , 0.33 W/m^2 , and 0.41 W/m^2 . The distribution of UVB had a skewness of -0.10 and kurtosis of -1.00 . The distribution was negatively tailed and was not Gaussian. Notably, 1204 days during the study period featured UVB values falling within the range of 0.3 W/m^2 to 0.4 W/m^2 .

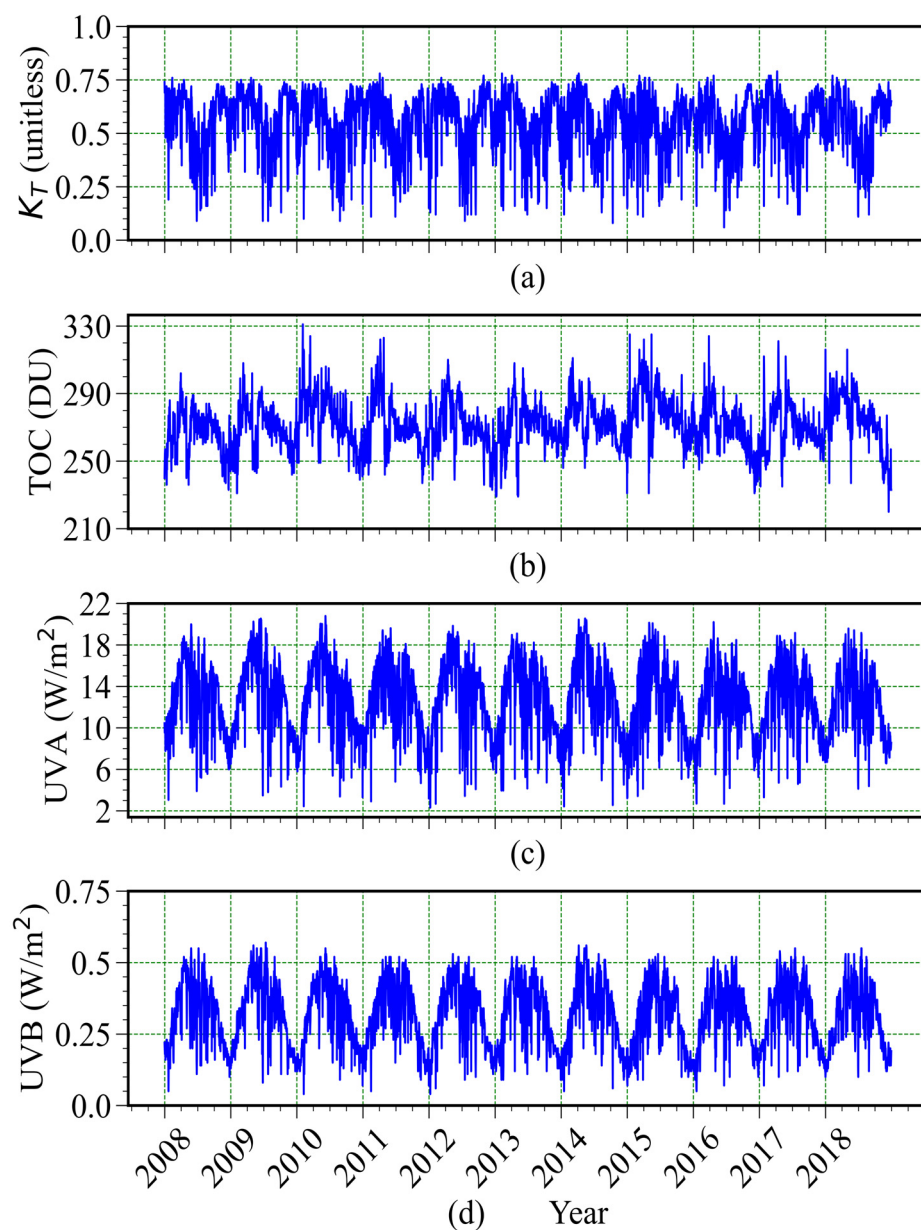


Figure 2. Daily variation in parameters: (a) clearness index, (b) TOC, (c) UVA, and (d) UVB.

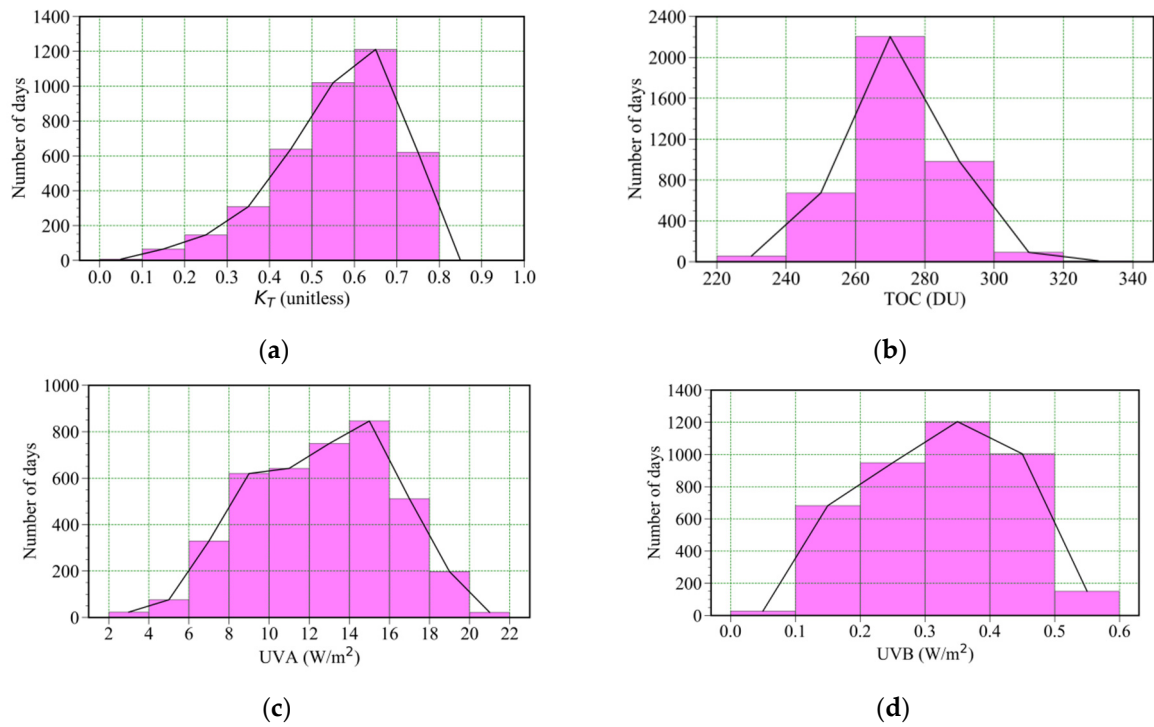


Figure 3. Histogram of parameters: (a) histogram of clearness index, (b) histogram of TOC, (c) histogram of UVA, and (d) histogram of UVB.

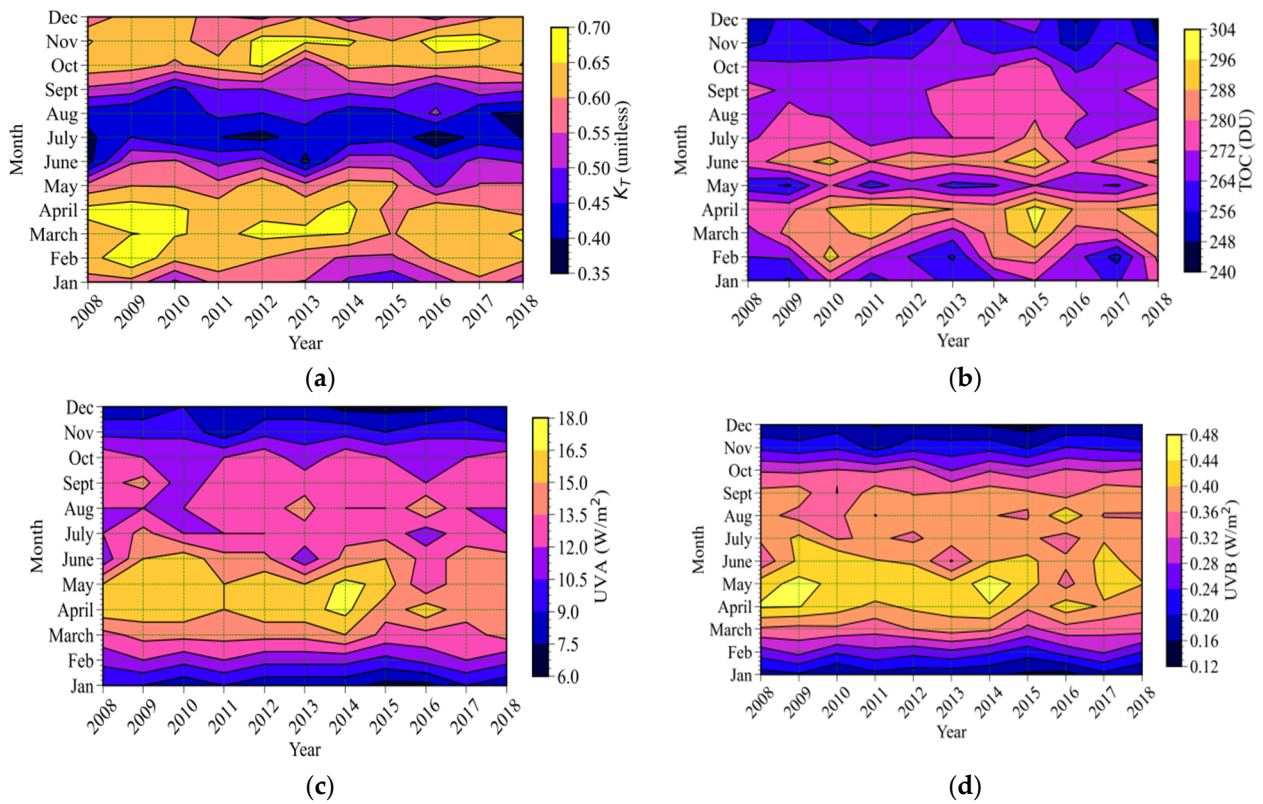


Figure 4. Monthly and annual variation in parameters: (a) K_T , (b) TOC (c) UVA, and (d) UVB.

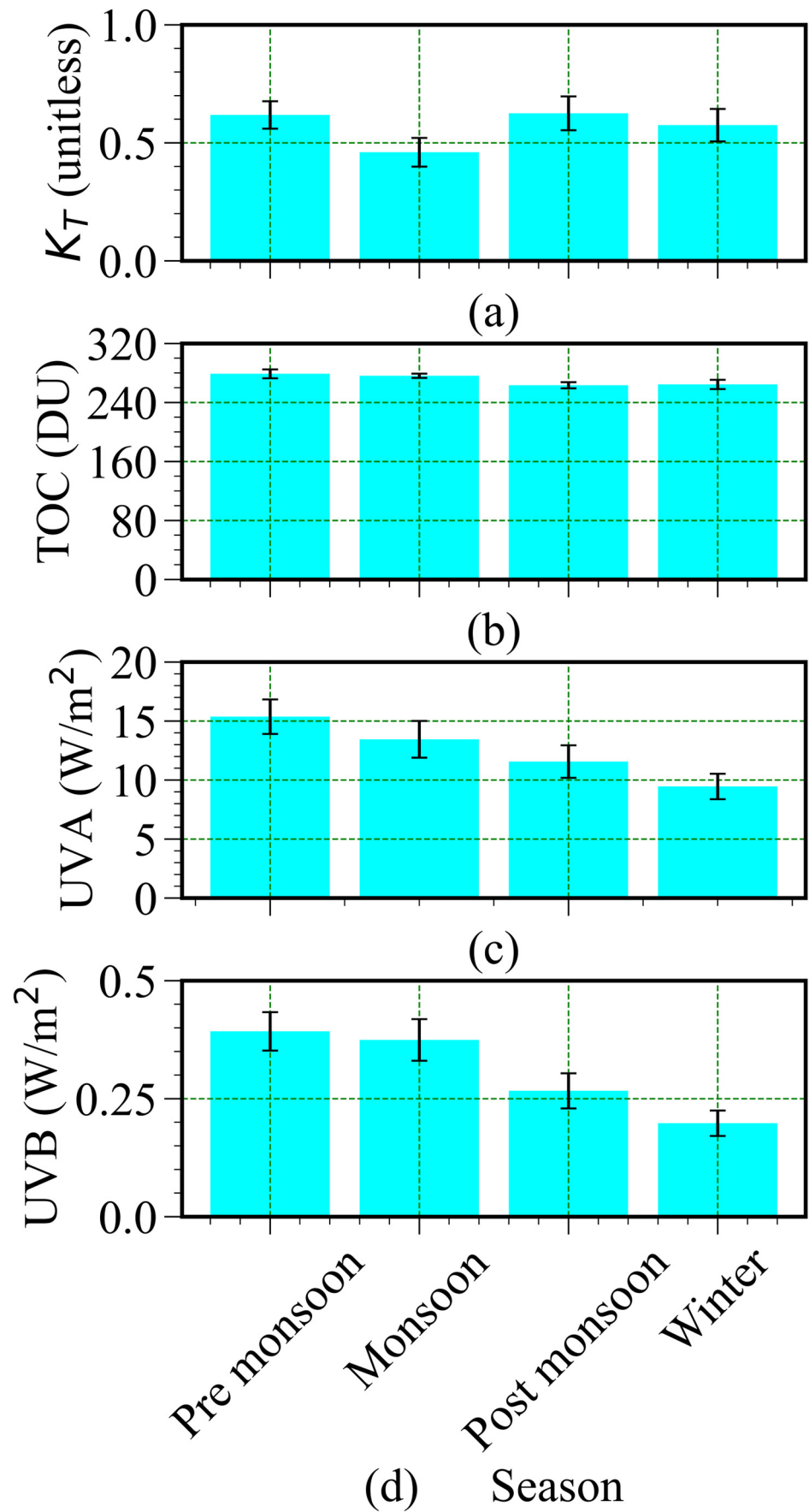


Figure 5. Seasonal variation in parameters (a) K_T , (b) TOC, (c) UVA, and (d) UVB.

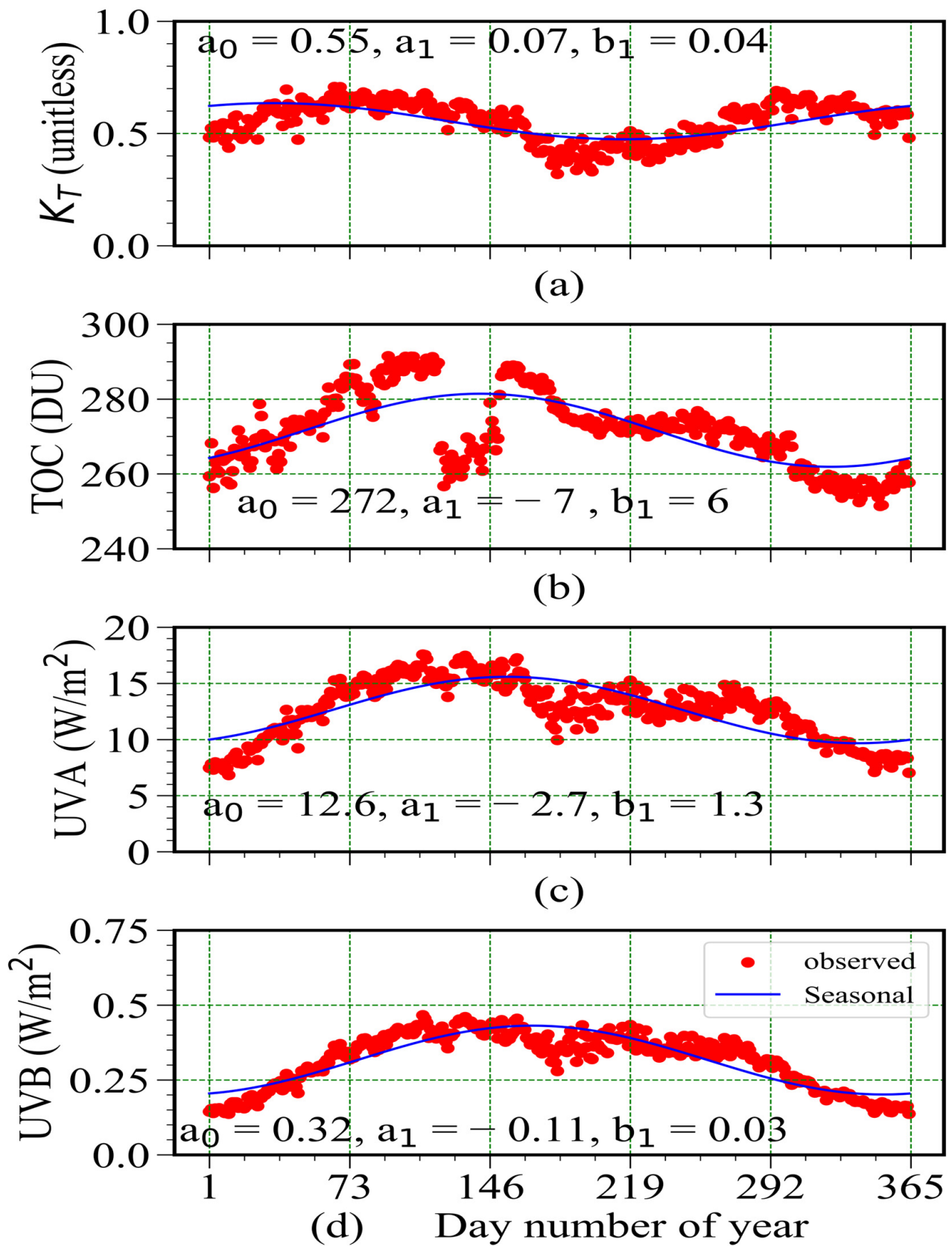


Figure 6. Fourier series of parameters: (a) clarity index, (b) TOC, (c) UVA, and (d) UVB.

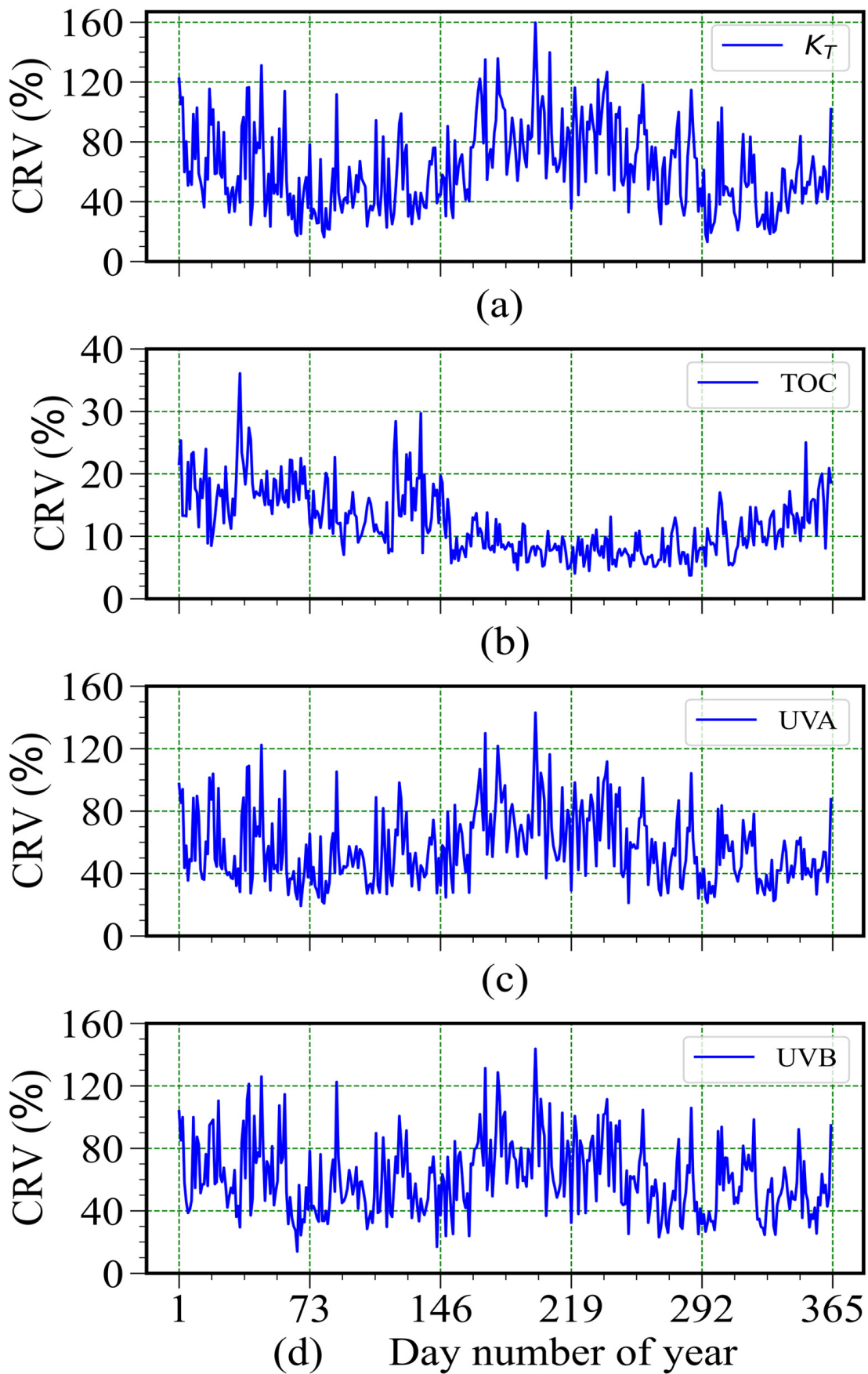


Figure 7. CRV of parameters: (a) clearness index, (b) TOC, (c) UVA, and (d) UVB.

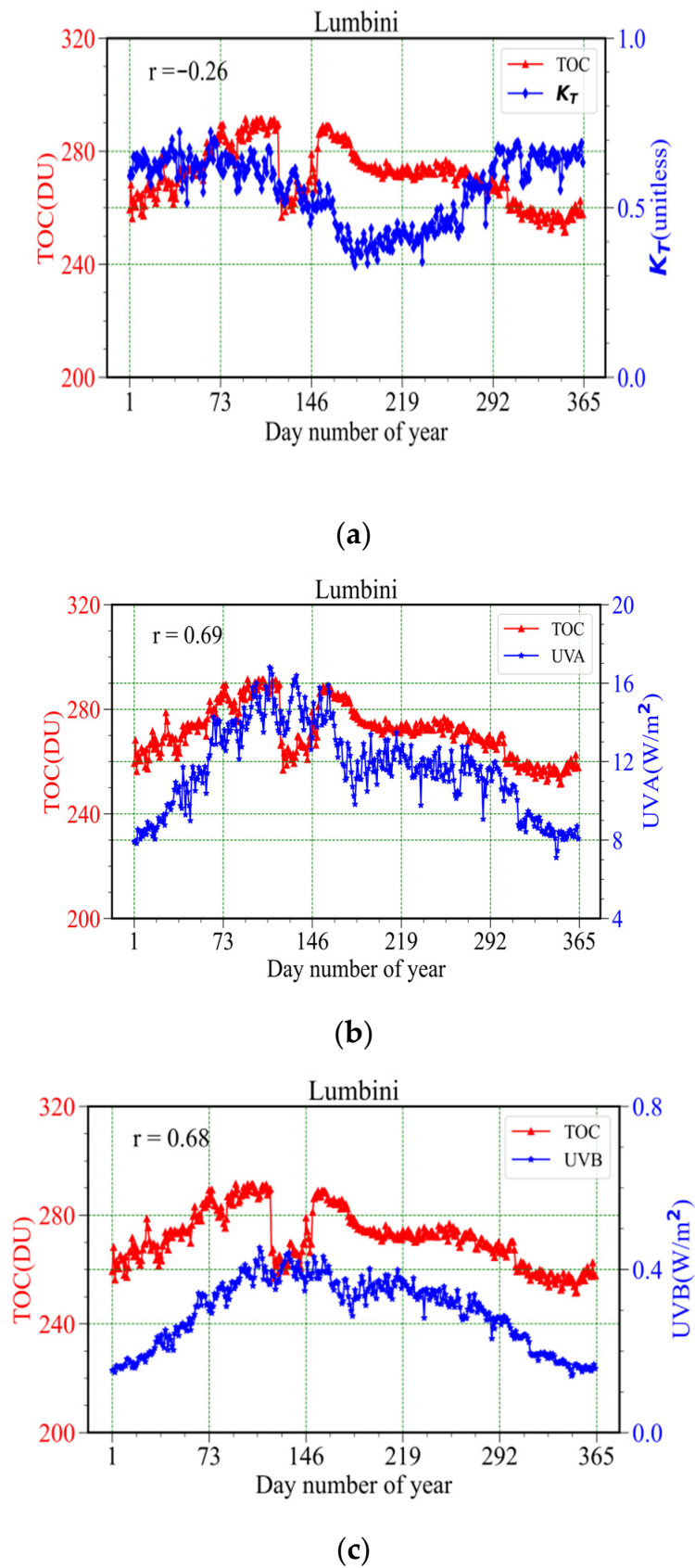


Figure 8. (a) Variation in clearness index and TOC. (b) Variation in UVA and TOC. (c) Variation in UVB and TOC.

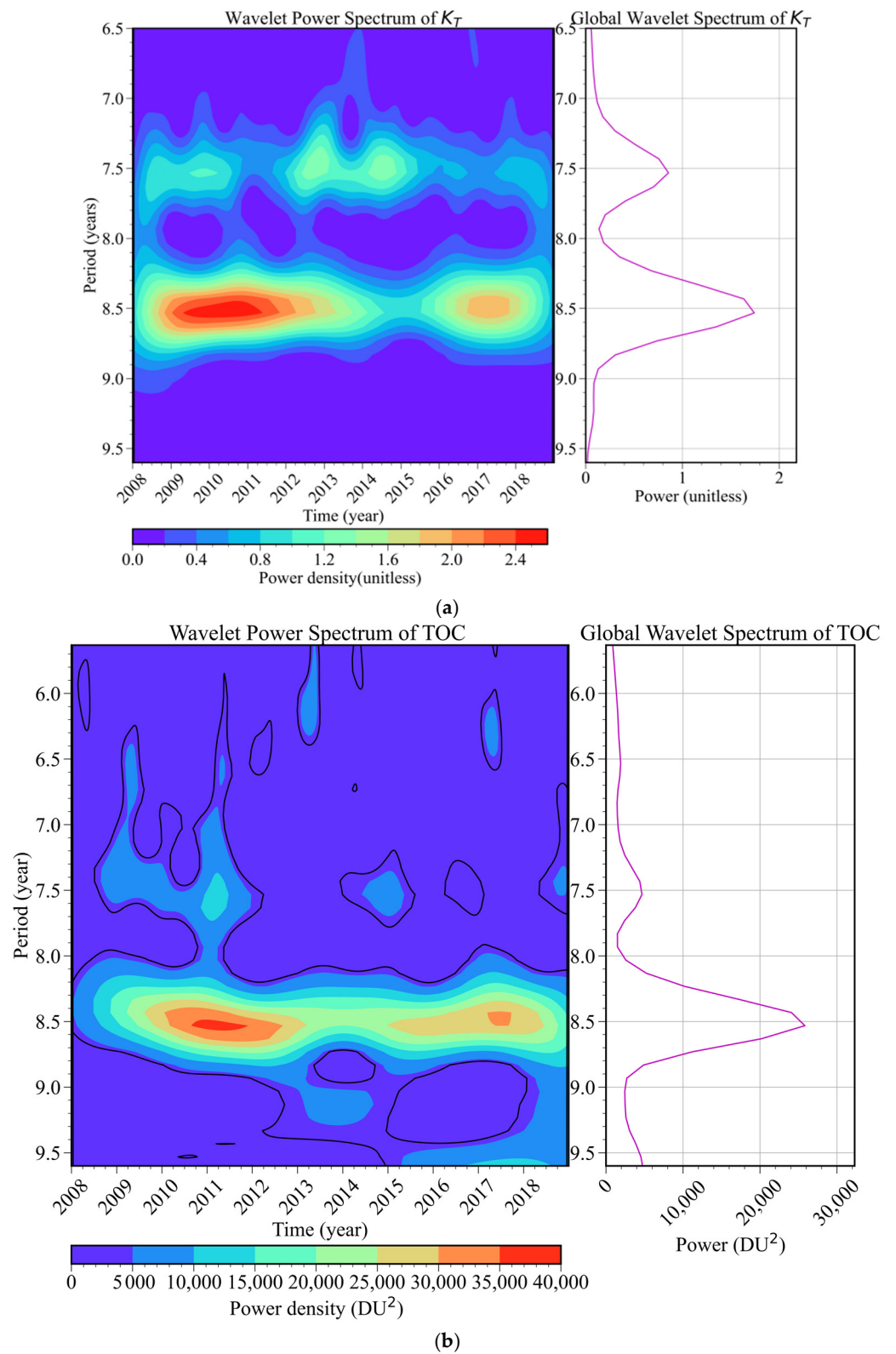


Figure 9. Cont.

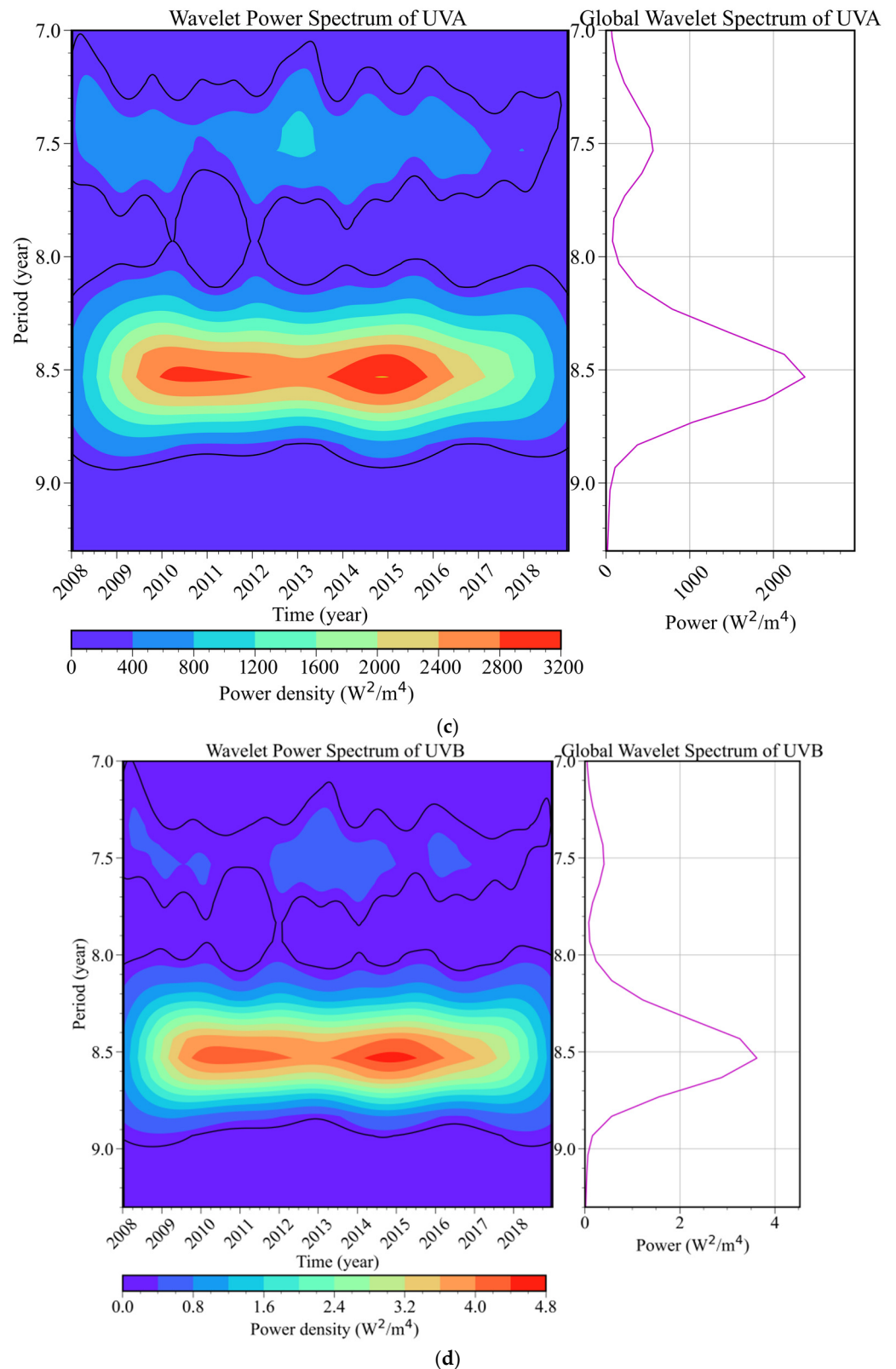


Figure 9. The continuous wavelet transform (CWT) parameters. (a) K_T . (b) TOC. (c) UVA. (d) UVB.

In Figure 3a, the negative skewness in the clearness index distribution indicates that more than 50 percent of the observed data points have values below the peak value of 0.6. This indicates a gradual decrease in atmospheric pollutants associated with improved air quality and increased atmospheric clarity. Factors contributing to this gradual decrease

in pollutants may include reduced emissions from anthropogenic sources (e.g., industrial activities, vehicular emissions) and natural processes (e.g., dispersion, precipitation). Like the clearness index, the negative skewness observed in the distributions of UVA and UVB radiation indicates a similar trend of decreasing atmospheric pollutants. Reduced levels of atmospheric pollutants allow ultraviolet radiation from the sun to penetrate more deeply, leading to higher UVA and UVB radiation levels reaching the Earth's surface. The positively skewed tail observed in the TOC distribution indicates a greater prevalence of higher TOC values. This positive skewness is attributed to the combined effect of tropospheric and stratospheric ozone. Stratospheric ozone, which is naturally occurring and primarily located in the stratosphere, contributes to higher TOC values. The distribution of the total ozone column (TOC) is skewed towards higher values due to the dominance of stratospheric ozone, with most days showing TOC measurements above 260 Dobson.

Figure 4 presents the annual and monthly variations in K_T , TOC, UVA, and UVB. Figure 4a illustrates the annual variation in the K_T , where the yearly average of the maximum K_T value during the 11-year study period is 0.58 ± 0.14 in 2009, with 154 clear days. The monthly average of the maximum K_T occurs in November at 0.64 ± 0.09 , featuring 192 clear days. Conversely, the annual average of the minimum K_T value is found to be 0.54 ± 0.13 in 2015, with 74 clear days, and the monthly average of the minimum is 0.43 ± 0.11 in July, with no clear days.

Figure 4b presents the annual variation in the TOC. Over the 11-year study period, the yearly average of the maximum TOC value is 280 ± 14 DU in 2015, and the monthly average of the maximum occurs in April at 289 ± 7 DU. The annual average of the minimum TOC value is 267 ± 12 DU in 2008, with the monthly average of the minimum at 257 ± 8 DU in December. Figure 4c depicts the annual UVA variation. The annual average of the maximum UVA value is 13.15 ± 3.51 W/m² in 2009, and the monthly average occurs in April at 15.92 ± 2.57 W/m². The yearly average of the minimum UVA value is 12.17 ± 3.36 W/m² in 2016, with the monthly average of the minimum at 8.29 ± 1.26 W/m² in December.

Similarly, Figure 4d illustrates the annual variation in UVB. The yearly average of the maximum UVB value is 0.33 ± 0.11 W/m² in 2009, with the monthly average of the maximum at 0.42 ± 0.07 W/m² in May. The annual average of the minimum UVB value is 0.30 ± 0.10 W/m² in 2015, with the monthly average of the minimum at 0.16 ± 0.02 W/m² in December. These comprehensive analyses provide valuable insights into atmospheric parameters' annual and monthly dynamics.

Figure 5 illustrates the seasonal changes in the K_T , TOC, UVA, and UVB. The seasonal variation in K_T is shown in Figure 5a. The maximum value of 0.62 ± 0.10 was recorded during the post-monsoon period (October and November), while the minimum value of 0.46 ± 0.12 was during the monsoon season (June, July, August, and September). This season, Nepal experiences the highest rainfall during the monsoon season, positively impacting the cleanliness of the atmosphere due to rain.

Looking at Figure 5b, we can see the seasonal changes in the TOC. The highest and lowest values recorded were 279 ± 10 DU during the pre-monsoon period (March, April, May) and 263 ± 6 DU during the post-monsoon period, respectively. Figure 5c shows the seasonal variation in UVA, with the highest and lowest values being 15.37 ± 2.52 W/m² during the pre-monsoon period and 9.45 ± 2.86 W/m² during the winter months (December, January, February), respectively. Finally, Figure 5d displays the seasonal variation in UVB, where the highest and lowest values recorded are 0.39 ± 0.07 W/m² during the pre-monsoon period and 0.19 ± 0.04 W/m² during the winter months, respectively.

Few previous studies present analysis of the TOC across various regions in Nepal, utilizing short-term datasets to gauge atmospheric ozone levels. In Kathmandu (27.72° N, 85.32° E, 1350 m), the observed average TOC from October 2004 to April 2016 was 268 DU [44]. Similarly, in Pokhara (28.22° N, 83.32° E, 850 m), observations from October 2008 to December 2010 indicated a TOC of 274.3 DU, whereas Biratnagar (26.45° N, 87.27° E, 72 m) exhibited a slightly higher average of 285.5 DU. In contrast, data from Jumla (29.28° N, 82.16° E, 2300 m) recorded between 2008 and 2014 showed an average TOC of

271.8 ± 14.1 DU [45,46]. Extending this body of work, our longitudinal study in Lumbini over eleven years (2008–2018) revealed a TOC of 279 ± 10 DU, underscoring the distinctive spatial variations in ozone concentration across different locales. This comparison suggests that proximity may not heavily influence TOC variations on a regional scale, despite non-simultaneous observations.

Figure 6 presents the Fourier series representations of the K_T , TOC, UVA, and UVB. For the K_T , the offset (a_0) was determined as 0.55, with an amplitude of the seasonal component ($\sqrt{a_1^2 + b_1^2}$) measuring 0.08. The offset and amplitude of the seasonal component of the TOC were 272 DU and 10 DU, respectively. During the pre-monsoon season, Lumbini experiences high temperatures. Changes in temperature gradients can influence wind patterns, affecting the transport of ozone-rich air masses and the overall ozone concentration. It is essential to understand the atmospheric chemistry of Lumbini, which is situated north of the Indo-Gangetic Plain. This region might have been affected by long-range transport of air pollution in this time, such as the transport of ozone-depleting substances (ODSs), as well as their precursor pollutants like nitrogen oxides (NOx) [23]. However, due to the lack of data on atmospheric chemical components, this study has yet to present data that connect lower observations of the TOC on days ranging from 110 to about 150 DOY.

The offset and amplitude of the seasonal component of UVA are 12.6 W/m^2 and 3.0 W/m^2 , respectively. The offset and amplitude of the seasonal component of UVB are 0.32 W/m^2 and 0.11 W/m^2 , respectively. The result shows that the seasonal variation in UVB is about 33%, in UVA is about 24%, and in clearness index is about 14%, whereas the seasonal variation in the TOC is only 4%. Previous studies have also indicated that the total amount of ozone in the atmosphere generally increases with latitude and is also affected by the season [32]. Also, the solar cycle plays a fundamental role in the variation in ozone concentrations [47].

Figure 7 illustrates the coefficient of relative variation (CRV) for K_T , TOC, UVA, and UVB. The maximum CRV value for the clearness index was observed at 160% on the 200th day of the year, attributed to a 50% coefficient of variance (CV) with large variation in the clearness index on that day.

The minimum CRV value was recorded at 13% on the 296th day of the year, associated with a 4% CV. There was a small variation in the clearness index on that day. The maximum value of CRV of the TOC was found to be 36% on the 35th day of the year due to a 9% CV, and the minimum value was 4% on the 286th day of the year due to the 1% CV. The maximum value of CRV of UVA was found to be 143% on the 200th day of the year due to the 44% CV, and the minimum value was 19% on the 69th day of the year due to the 9% CV. The maximum value of CRV of UVB was 144% on the 200th day of the year due to the 46% CV, and the minimum value was 14% on the 67th day of the year due to the 4% CV.

Figure 8 shows the variation in the TOC with K_T , UVA, and UVB. Here, the correlation coefficient (r) was used to find the relation between two variables. There was no significant effect of the clearness index on the TOC, but there was a positive effect of UVA and UVB on the TOC. Lumbini, a nearby place in the IGP region, experiences changes in seasonal aerosol levels. Studies have shown that aerosol levels are highest during the post-monsoon and pre-monsoon periods, followed by winter, while the lowest levels occur during the monsoon season [48]. However, cloud cover is highest during the monsoon (June to September) and lowest during the pre- and post-monsoon [49]. As shown in Figure 8a, the K_T parameter with a minimum in summer and higher values during the pre- and post-monsoon indicate that it is strongly affected by clouds rather than by air quality.

In Figure 9, the continuous wavelet transform (CWT) of the K_T , TOC, UVA, and UVB is presented. Figure 9a shows the wavelet power spectrum (WPS) and Global wavelet power spectrum GWS of the K_T . A power density of K_T greater than 2.4 was recorded from mid-2009 to 2011 in an 8.5-year period. This is also shown in the global wavelet spectrum (GWS). From 2011 to 2018, the power density of K_T is observed greater than 1.0 in that 8.5-year period and with closer to 2.0 from the end of 2016 to the end of 2017, respectively. Figure 9b shows the WPS and GWS of the TOC. The power density of the TOC recorded

from the end of 2010 to the end of 2011 was about 35,000 DU². This is also shown in the GWS. From mid-2017 to the start of 2018, the power density of the TOC was between 30,000 and 35,000 DU² in the 8.5-year period. Figure 9c shows the WPS and GWS of UVA. The power density of UVA recorded from 2010 to 2012 and 2014 to the end of 2015 was greater than 2800 (W/m²). This is also shown in the GWS. Figure 9d shows the WPS and GWS of UVB. A power density of UVB greater than 4.6 (W/m²) was recorded from 2010 to mid-2012 and mid-2014 to mid-2015 over an 8.5-year period. This periodicity demonstrates the complex interplay the broader atmospheric processes.

4. Conclusions

The comprehensive analysis of K_T , TOC, UVA, and UVB over Lumbini, Nepal, provides valuable insights into the dynamics of solar radiation and climatic variations in the region. The observed patterns contribute to understanding the significance of seasonal variations in K_T , TOC, UVA, and UVB levels and highlight the influence of meteorological factors such as the monsoon season on atmospheric composition and radiation levels in an 8.5-year period.

The study revealed distinct patterns of K_T that varied daily, monthly, and seasonally, providing vital information on the frequency of clear, cloudy, and partially clear days. Seasonal changes in clearness index levels indicate the impact of the monsoon and post-monsoon seasons on solar radiation levels, as evidenced by seasonal variations, and the post-monsoon months of October and November exhibited the highest K_T values (0.62 ± 0.10), while the monsoon months of June, July, August, and September showed the lowest values (0.40 ± 0.12). The TOC showed variations over time, with a peak of 331 DU in 2010 and a minimum of 220 DU in 2018. The results also revealed that the TOC values were higher during the pre-monsoon season (March, April, and May) at an average of 279 ± 10 DU, while lower values were observed during the post-monsoon period. Thus, the total ozone content displayed annual and seasonal variations, with notable extremes in maximum and minimum levels. The study highlighted the significant contribution of the pre-monsoon period to elevated TOC levels. A comprehensive comparison of the chemical components of air pollution data and other climatic conditions related to the ozone interaction that will enhance our further understanding with a clear picture of a sudden decrease over a few days in the pre-monsoon season, particularly on days 110 to 150 of the year, to identify the factors responsible for the lower levels of TOC during these days.

Seasonal variations in UVA and UVB levels provide valuable insights into the impact of various seasons on ultraviolet radiation exposure, which can be observed from the daily variation in UVA, which ranged from 2.31 to 20.79 W/m², with notable occurrences of UVA between 14 W/m² and 16 W/m² for 846 days. Seasonal patterns indicated higher UVA and UVB values in the pre-monsoon and lower ones in winter. Fourier series analysis highlighted an offset of 12.6 W/m² and an amplitude of 3.0 W/m² for UVA, an offset of 0.32 W/m², and an amplitude of 0.11 W/m² for UVB. The Fourier series analysis of the clearness index, TOC, UVA, and UVB provides a mathematical framework to discern the seasonal components, offering essential parameters such as offset and amplitude. These analytical outcomes contribute to a refined understanding of cyclic patterns and trends within the studied atmospheric variables.

Author Contributions: P.M.S.: developing concept, methodology, writing—original draft: S.P.G., U.J., M.S., R.A., B.R.T., B.A., N.P.C., I.B.K. and K.N.P.: conceptualization, review, analyzing methodology, writing, and editing. All authors have read and agreed to the published version of the manuscript.

Funding: This research received no external funding.

Institutional Review Board Statement: Not applicable.

Informed Consent Statement: Not applicable.

Data Availability Statement: Data available in a publicly accessible repository that does not issue DOIs Publicly available datasets were analyzed in this study. This data can be found here: [<https://data.ceda.ac.uk/badc/toms/data/omi> and <https://power.larc.nasa.gov>] accessed on: 13 April 2024.

Acknowledgments: The authors would like to convey their gratitude to the faculty of the Central Department of Physics, Patan Multiple Campus, IoST, for this opportunity as well as NASA and CEDA for the data. We sincerely appreciate NAST for the PhD fellowship for Prakash Shrestha, and Franklin Pierce University for providing the research support funds to author Rudra Aryal for this collaborative research work. We would also like to acknowledge Nepal Physical Society (NPS) and the Association of Nepali Physicists in America (ANPA) for the educational workshop on Python.

Conflicts of Interest: The authors declare no conflict of interest.

References

1. Alebrahim, M.A.; Bakkar, M.M.; Al Darayseh, A.; Msameh, A.; Jarrar, D.; Aljabari, S.; Khater, W. Awareness and Knowledge of the Effect of Ultraviolet (UV) Radiation on the Eyes and the Relevant Protective Practices: A Cross-Sectional Study from Jordan. *Healthcare* **2022**, *10*, 2414. [[CrossRef](#)]
2. IARC Working Group on the Evaluation of Carcinogenic Risks to Humans. *Radiation*. Lyon (FR): International Agency for Research on Cancer; 2012. (IARC Monographs on Evaluating Carcinogenic Risks to Humans, No. 100D.) "SOLAR AND ULTRAVIOLET RADIATION". Available online: <https://www.ncbi.nlm.nih.gov/books/NBK304366/> (accessed on 5 March 2024).
3. Bornman, J.F.; Barnes, P.W.; Robson, T.M.; Robinson, S.A.; Jansen, M.A.K.; Ballaré, C.L.; Flint, S.D. Linkages between stratospheric ozone, uv radiation and climate change and their implications for terrestrial ecosystems. *Photochem. Photobiol. Sci.* **2019**, *18*, 681–716. [[CrossRef](#)]
4. Dale Wilson, B.; Moon, S.; Armstrong, F. Comprehensive Review of Ultraviolet Radiation and the Current Status on Sunscreens. *J. Clin. Aesthet. Dermatol.* **2012**, *5*, 18–23.
5. Batakliiev, T.; Georgiev, V.; Anachkov, M.; Rakovsky, S.; Zaikov, G.E. Ozone Decomposition. *Interdiscip. Toxicol.* **2014**, *7*, 47–59. [[CrossRef](#)]
6. Volz, A.; Kley, D. Evaluation of the montsouris series of ozone measurements made in the nineteenth century. *Nature* **1988**, *332*, 240–242. [[CrossRef](#)]
7. World Health Organization. Available online: [https://www.who.int/news-room/questions-and-answers/item/radiation-ultraviolet-\(uv\)](https://www.who.int/news-room/questions-and-answers/item/radiation-ultraviolet-(uv)) (accessed on 5 March 2024).
8. EPA United States Protection Agency. Available online: <https://www.epa.gov/ozone-layer-protection/frequently-asked-questions-about-ozone-layer#section1> (accessed on 5 March 2024).
9. Herman, J.R.; Hudson, R.; McPeters, R.; Stolarski, R.; Ahmad, Z.; Gu, X.Y.; Taylor, S.; Wellemeyer, C. A new selfcalibration method applied to toms and sbuv backscattered ultraviolet data to determine long-term global ozone change. *J. Geophys. Res. Atmos.* **1991**, *96*, 7531–7545. [[CrossRef](#)]
10. Kudish, A.; Ianetz, A. Analysis of the solar radiation data for Beer Sheva, Israel, and its environs. *Sol. Energy* **1992**, *48*, 97–106. [[CrossRef](#)]
11. Ogawa, T.; Miyata, A. Seasonal behavior of the tropospheric ozone in Japan. In *Atmospheric Ozone: Proceedings of the Quadrennial Ozone Symposium Held in Halkidiki, Greece 3–7 September 1984*; Springer: Berlin/Heidelberg, Germany, 1985; pp. 754–758. [[CrossRef](#)]
12. Monks, P.S.; Archibald, A.T.; Colette, A.; Cooper, O.; Coyle, M.; Derwent, R.; Fowler, D.; Granier, C.; Law, K.S.; Mills, G.E.; et al. Tropospheric ozone and its precursors from the urban to the global scale from air quality to short-lived climate forcer. *Atmos. Chem. Phys.* **2015**, *15*, 8889–8973. [[CrossRef](#)]
13. Ramanathan, V.; Ramana, M.V.; Roberts, G.; Kim, D.; Corrigan, C.; Chung, C.; Winker, D. Warming trends in asia amplified by brown cloud solar absorption. *Nature* **2007**, *448*, 575–578. [[CrossRef](#)]
14. Bernhard, G.H.; Neale, R.E.; Barnes, P.W.; Neale, P.J.; Zepp, R.G.; Wilson, S.R.; Andrady, A.L.; Bais, A.F.; McKenzie, R.L.; Aucamp, P.J.; et al. Environmental Effects of Stratospheric Ozone Depletion, UV Radiation and Interactions with Climate Change: UNEP Environmental Effects Assessment Panel, Update 2019. *Photochem. Photobiol. Sci.* **2020**, *19*, 542–584. [[CrossRef](#)]
15. Wang, H.; Lu, X.; Jacob, D.J.; Cooper, O.R.; Chang, K.-L.; Li, K.; Gao, M.; Liu, Y.; Sheng, B.; Wu, K.; et al. Global Tropospheric Ozone Trends, Attributions, and Radiative Impacts in 1995–2017: An Integrated Analysis Using Aircraft (IAGOS) Observations, Ozonesonde, and Multi-Decadal Chemical Model Simulations. *Atmos. Chem. Phys.* **2022**, *22*, 13753–13782. [[CrossRef](#)]
16. United Nations Environment Programme. Integrated Assessment of Black Carbon and Tropospheric Ozone: Summary for Decision Makers. 2011. Available online: <https://wedocs.unep.org/20.500.11822/8028> (accessed on 13 April 2024).
17. Andreae, M.O.; Ramanathan, V. Climate's dark forcings. *Science* **2013**, *340*, 280–281. [[CrossRef](#)]
18. Bond, T.C.; Doherty, S.J.; Fahey, D.W.; Forster, P.M.; Berntsen, T.; DeAngelo, B.J.; Flanner, M.G.; Ghan, S.; Kärcher, B.; Koch, D.; et al. Bounding the role of black carbon in the climate system: A scientific assessment. *J. Geophys. Res. Atmos.* **2013**, *118*, 5380–5552. [[CrossRef](#)]
19. Stolarski, R.; Bojkov, R.; Bishop, L.; Zerefos, C.; Staehelin, J.; Zawodny, J. Measured trends in stratospheric ozone. *Science* **1992**, *256*, 342–349. [[CrossRef](#)]

20. Harris, N.R.P.; Ancellet, G.; Bishop, L.H.; Hofmann, D.J.; Kerr, J.B.; McPeters, R.D.; Prendez, M.; Randel, W.J.; Staehelin, J.; Subbaraya, B.H.; et al. Trends in stratospheric and free tropospheric ozone. *J. Geophys. Res. Atmos.* **1997**, *102*, 1571–1590. [[CrossRef](#)]
21. Ackerman, M.; Muller, C. Stratospheric Methane and Nitrogen Dioxide from Infrared Spectra. *Pure Appl. Geophys.* **1973**, *106*, 1325–1335. [[CrossRef](#)]
22. Seinfeld, J.H.; Pandis, S.N. *Atmospheric Chemistry and Physics: From Air Pollution to Climate Change*; John Wiley & Sons: Hoboken, NJ, USA, 2016.
23. Berezina, E.; Moiseenko, K.; Skorokhod, A.; Pankratova, N.V.; Belikov, I.; Belousov, V.; Elansky, N.F. Impact of VOCs and NO_x on Ozone Formation in Moscow. *Atmosphere* **2020**, *11*, 1262. [[CrossRef](#)]
24. Bittencourt, G.D.; Pinheiro, D.K.; Bencherif, H.; Begue, N.; Peres, L.V.; Bageston, J.V.; da Silva, F.R.; de Bem, D. Multi-Instrumental Analysis of Ozone Vertical Profile and Total Column in South America: Comparison between Subtropical and Equatorial Latitudes. *EGUosphere* **2023**, *1*, 1664.
25. Zeng, Y.; Zhang, J.; Li, Y.; Liu, S.; Chen, H. Wavelet Analysis of Ozone Driving Factors Based on ~20 Years of Ozonesonde Measurements in Beijing. *Atmosphere* **2023**, *14*, 1733. [[CrossRef](#)]
26. Mbatha, N.; Bencherif, H. Time Series Analysis and Forecasting Using a Novel Hybrid LSTM Data-Driven Model Based on Empirical Wavelet Transform Applied to Total Column of Ozone at Buenos Aires, Argentina (1966–2017). *Atmosphere* **2020**, *11*, 457. [[CrossRef](#)]
27. Peled, A.; Appelbaum, J. Evaluation of Solar Radiation Properties by Statistical Tools and Wavelet Analysis. *Renew. Energy* **2013**, *59*, 30–38. [[CrossRef](#)]
28. Rupakheti, D.; Adhikary, B.; Praveen, P.S.; Rupakheti, M.; Kang, S.; Mahata, K.S.; Naja, M.; Zhang, Q.; Panday, A.K.; Lawrence, M.G. Pre-monsoon air quality over Lumbini, a world heritage site along the Himalayan foothills. *Atmos. Chem. Phys.* **2017**, *17*, 11041–11063. [[CrossRef](#)]
29. Rupakheti, D.; Kang, S.; Rupakheti, M. Two heavy haze events over Lumbini in southern Nepal: Enhanced aerosol radiative forcing and heating rates. *Atmosphere* **2020**, *11*, 658. [[CrossRef](#)]
30. Kumari, S.; Lakhani, A.; Kumari, K.M. First Observation-Based Study on Surface O₃ Trend in Indo-Gangetic Plain: Assessment of Its Impact on Crop Yield. *Chemosphere* **2020**, *255*, 126972. [[CrossRef](#)] [[PubMed](#)]
31. Qu, Y.; Voulgarakis, A.; Wang, T.; Kasoar, M.; Wells, C.; Yuan, C.; Varma, S.; Mansfield, L. A Study of the Effect of Aerosols on Surface Ozone Through Meteorology Feedbacks over China. *Atmos. Chem. Phys.* **2021**, *21*, 5705–5718. [[CrossRef](#)]
32. Regmi, J.; Poudyal, K.N.; Pokhrel, A.; Gyawali, M.; Tripathi, L.; Panday, A.; Barinelli, A.; Aryal, R. Investigation of Aerosol Climatology and Long-Range Transport of Aerosols over Pokhara, Nepal. *Atmosphere* **2020**, *11*, 874. [[CrossRef](#)]
33. Zhu, T.; Deng, H.; Huang, J.; Zheng, Y.; Li, Z.; Zhao, R.; Wang, H. Analysis of Ozone Vertical Profiles over Wuyishan Region during Spring 2022, and Their Correlations with Meteorological Factors. *Atmosphere* **2022**, *13*, 1505. [[CrossRef](#)]
34. Survey Department, Government of Nepal. Available online: <https://dos.gov.np/downloads/nepal-map> (accessed on 31 December 2023).
35. CBS. *Environment Statistics of Nepal 2019*; Central Bureau of Statistics, National Planning Commission Secretariat, Government of Nepal: Kathmandu, Nepal, 2019.
36. CEDA ARCHIVE. Available online: <https://data.ceda.ac.uk/badc/toms/data/omi/> (accessed on 7 January 2024).
37. The Power Project. Available online: <https://power.larc.nasa.gov/> (accessed on 31 December 2023).
38. ANACONDA. Available online: <https://www.anaconda.com/download> (accessed on 10 September 2023).
39. Spiegel, M.R.; Stephens, L.J. *Schaum's Outline of Theory and Problems of Statistics*; Schaum's Outline Series; McGraw-Hill: New York, NY, USA, 1998; ISBN 0-07-060281-6.
40. Anton, M.; Bortoli, D.; Costa, M.J.; Kulkarni, P.S.; Domingues, A.F.; Barriopedro, D.; Serrano, A.; Silva, A.M. Temporal and Spatial Variabilities of Total Ozone Column over Portugal. *Remote Sens. Environ.* **2011**, *115*, 855–863. [[CrossRef](#)]
41. Sonechkin, D.M.; Datsenko, N.M. Wavelet Analysis of Nonstationary and Chaotic Time Series with an Application to the Climate Change Problem. In *Fractals and Dynamic Systems in Geoscience*; Springer: Berlin/Heidelberg, Germany, 2000; pp. 653–677. [[CrossRef](#)]
42. Torrence, C.; Compo, G.P. A Practical Guide to Wavelet Analysis. *Bull. Am. Meteorol. Soc.* **1998**, *79*, 61–78. [[CrossRef](#)]
43. Falayi, E.O.; Adepitan, J.O.; Adewole, A.T.; Roy-Layinde, T.O. Analysis of Rainfall Data of Some West African Countries Using Wavelet Transform and Nonlinear Time Series Techniques. *J. Spat. Sci.* **2023**, *68*, 385–396. [[CrossRef](#)]
44. Chapagain, N.P. Total ozone content over Kathmandu from TOMS observations. *Int. J. Eng. Res. Appl.* **2016**, *6*, 69–75.
45. Shrestha, P.M.; Chapagain, N.P.; Karki, I.B.; Poudyal, K.N. Study of variability of atmospheric ozone over Jumla in a half period of 24 solar cycles. *J. Nepal Phys. Soc.* **2021**, *7*, 31–38. [[CrossRef](#)]
46. Sharma, R.R.; Kjeldstad, B.; Bhattarai, B.K. Comparison of UV Index and Total Ozone Column of Aura/OMI and Ground Measurement from Nepal Himalayas. *J. Inst. Eng.* **2011**, *8*, 114–129. [[CrossRef](#)]
47. Shindell, D.T.; Rind, D.; Balachandran, N.; Lean, J.; Lonergan, P. Solar Cycle Variability, Ozone and Climate. *Science* **1999**, *284*, 305–308. [[CrossRef](#)]

-
48. Rupakheti, D.; Kang, S.; Rupakheti, M.; Cong, Z.; Tripathee, L.; Panday, A.K.; Holben, B.N. Observation of optical properties and sources of aerosols at Buddha's birthplace, Lumbini, Nepal: Environmental implications. *Environ. Sci. Pollut. Res. Int.* **2018**, *25*, 14868–14881. [[CrossRef](#)]
 49. Meteoblue. Simulated Historical Climate & Weather Data for Lumbini. Available online: https://www.meteoblue.com/en/weather/historyclimate/climatemodelled/lumbini_nepal_1282839/ (accessed on 10 April 2024).

Disclaimer/Publisher's Note: The statements, opinions and data contained in all publications are solely those of the individual author(s) and contributor(s) and not of MDPI and/or the editor(s). MDPI and/or the editor(s) disclaim responsibility for any injury to people or property resulting from any ideas, methods, instructions or products referred to in the content.